Synchronized Operando Analysis of Graphite Negative Electrode of Li-Ion Battery

Journal of The Electrochemical Society, 2021 **168** 080508

Synchronized Operando Analysis of Graphite Negative Electrode of Li-Ion Battery

Hiroyuki Fujimoto,[1,z] Miwa Murakami,[1] Toshiro Yamanaka,[1] Keiji Shimoda,[1] Hisao Kiuchi,[1] Zempachi Ogumi,[1,*] and Takeshi Abe[2,]**

[1]*Office of Society-Academia Collaboration for Innovation, Kyoto University, Kyoto 611-0011, Japan*
[2]*Graduate School of Global Environmental Studies, Kyoto University, Kyoto 615-8510, Japan*

Since the rechargeable Li-ion battery was invented in the early 1990s, its performance has evolved continually and Li-ion batteries are now installed in most mobile devices. In these batteries, graphite is used as a negative electrode material. However, the detailed reaction mechanism between graphite and Li remains unclear. Here we apply synchrotron X-ray diffraction, ^{7}Li-nuclear magnetic resonance and Raman spectroscopy to operando analysis of the charge/discharge mechanism of a graphite electrode. The spectrum of the graphite electrode is measured repeatedly during the reaction. The operando dataset obtained is then analyzed synchronously with the composition of x in LiC_x estimated from the charge/discharge curves. We propose a synchronized operando analysis method that provides useful information about the behavior of the C–C bond vibration mode and the interactions between Li and carbon atoms due to structural change during the charge/discharge reaction. In addition, we determine details of the intercalation mechanism.

 [DOI: 10.1149/1945-7111/ac18e4]

Manuscript submitted June 24, 2021; revised manuscript received July 12, 2021. Published August 6, 2021.

Approximately 30 years have passed since initial commercialization of lithium-ion batteries using graphite negative electrode materials. However, the charge/discharge mechanism has yet to be clarified. The fundamental negative electrode reaction mechanism involves formation of a Li-graphite intercalation compound (Li-GIC). Initially, Li ions intercalate into each interlayer of the graphite to form dilute stage 1. This stage then transitions to a higher stage structure (Fig. A·1). Finally, when fully intercalated (Li ions inserted between all layers), the stage 1 structure is formed via stages 3 and 2. Stage 1 and 2 compound structures were established previously.[1–6] Both have the same in-plane structure defined by p($\sqrt{3} \times \sqrt{3}$)R30°, as shown in Fig. 1, structure E.[2,3] In the in-plane superlattice notation, p denotes a primitive unit cell, ($i \times j$) denotes unit vectors measured in units of $a_0 = 0.24612$ nm in each hexagonal lattice primitive cell of graphite in Fig. 1, structure A, and Rθ denotes the rotation angle of the superlattice unit vectors relative to the graphite unit vectors. Billaud et al. prepared several Li-GICs at different stages and indexed 00l diffractions for stages 1 to 5, finding another stage 2 compound (LiC_{18}) with an in-plane structure of p(3 × 3)R0°, as shown in Fig. 1, structure D.[7,8] This structure's in-plane composition was LiC_9. Dahn investigated Li-ion battery charge/discharge products via X-ray diffraction and reported that Li ions initially intercalated between all interlayers to form a dilute stage 1 that differed stoichiometrically[9] from the conventional stage 1. This structure then evolved from dilute stage 1 to stages 4 and 3, liquid-type stage 2 l and finally LiC_6-type stages 2 and 1 with increasing Li concentration. No stage beyond 4 was observed. Since Dahn's report, several researchers have discussed his paper.[10–15] Inaba et al. analysed the charge/discharge products using in situ Raman spectroscopy and obtained similar results.[10] However, their failure to observe the in-plane LiC_9 structure or stages above 5 contradicted the results of Billaud et al. Ohzuku reported a maximum stage number of 8 with an in-plane LiC_9 structure.[11] Zaghib et al. also observed stage 8 with a LiC_{72} composition via ^{7}Li-nuclear magnetic resonance (NMR) measurements.[12]

Since 2000, the "operando" observation technique has used methods including neutron diffraction and synchrotron X-ray diffraction (SXD) to elucidate detailed Li-GIC reaction mechanisms during charging/discharging.[16–25] Yazami and Reynier tracked structural changes during charging and discharging via X-ray diffraction and observed hysteresis in these changes.[13] Mathiesen et al. measured the graphite 002 and $hk0$ diffraction lines using SXD and tracked stage structural changes and in-plane structural changes.[25] Similar operando measurement techniques have been applied to NMR spectroscopy. Letellier and Chevallier reported LiC_{6n} and LiC_{9n} structure formation during charge/discharge processes.[14,15] Krachkovskiy et al. and Freytag et al. observed dilute stage structure signals using ^{7}Li-NMR.[26,27] Because techniques such as SXD, ^{7}Li-NMR and Raman spectroscopy have different measurement principles, they provide multifaceted information about the charge/discharge mechanism, including dynamic structural changes, interactions between Li and carbon atoms and C-C bond vibration changes. Therefore, if these operando analyses are performed using the same graphite electrode under identical charge/discharge conditions, the dataset can be analysed synchronously as a function of composition x in LiC_x estimated from the charge/discharge curves to provide more effective information. Recently, we performed SXD-based operando observations during graphite electrode charge/discharge processes in Li-ion batteries and presented detailed analyses of the Bragg d values of the 002, 101 and 100 diffractions of graphite.[28] Several inflections appeared in the d value plot as a function of x in LiC_x when x was near a multiple of 6, 9 or 72. Finally, we proposed a new in-plane LiC_{72n} (n = 1, 2) superlattice structure in addition to LiC_{6n} (n = 1, 2) and LiC_{9n} (n = 3–8) and summarized the relationship between the stage structures and in-plane superlattices, as shown in Fig. 1. To confirm this charge/discharge reaction mechanism, here we present a synchronized operando analysis concept using SXD, ^{7}Li-NMR and Raman spectroscopy and perform the proposed analysis for the graphite electrode of a Li-ion battery.

Experimental

To perform operando measurements using SXD, ^{7}Li-NMR and Raman spectroscopy, three types half-cell composed of graphite and Li-metal electrodes were assembled with an electrolyte of 1 mol·dm^{-3}-$LiPF_6$/ethylene carbonate + ethyl methyl carbonate (3:7) (Fig. 2). Because the measurement principles are different for each process, it is impossible to perform the measurements simultaneously. Therefore, each operando measurement is performed independently using the same graphite electrode under identical charge/discharge conditions and the successively obtained spectral datasets were analysed synchronously with the charge/discharge curves, the

*Electrochemical Society Fellow.
**Electrochemical Society Member.
[z]E-mail: fujimoto.hiroyuki.5n@kyoto-u.ac.jp

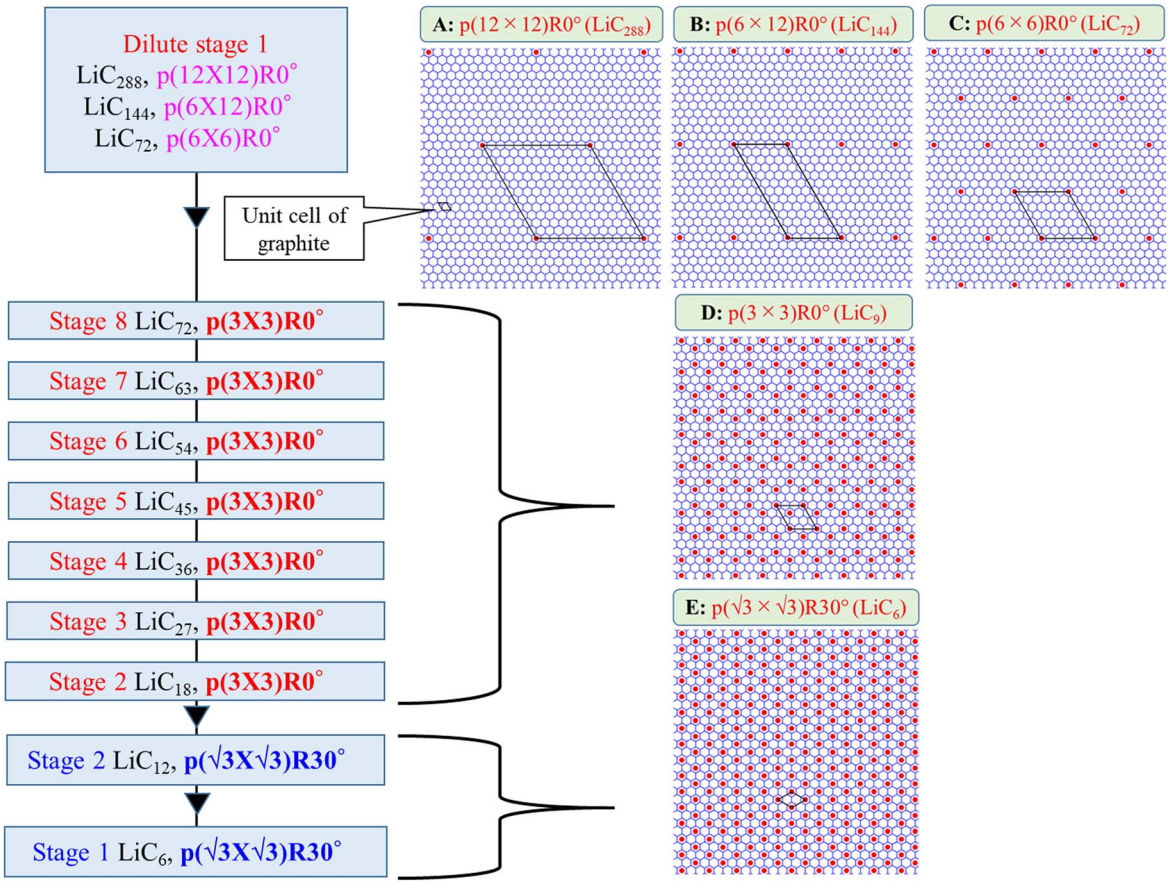

Figure 1. Relationship between the stage structures and in-plane superlattices of Li-GIC. Rearrangement of the superlattice proceeds in the order of A → B → C → D → E and, in conjunction with this process, the stage structures change in the order of dilute stage 1 → stage 8 → stage 7 → stage 6 → stage 5 → stage 4 → stage 3 → stage 2 → stage 1.

differential curves for the electric potential V (V-dQ/dV) and the LiC_x compositions calculated from Q. As the starting electrode material and electrolyte for the operando analysis, natural graphite (OMAC-R 1.0Z with a median diameter of 18 μm, Osaka Gas Chemical Co., Ltd. Japan) and 1 mol·dm^{-3}-$LiPF_6$/ethylene carbonate + ethyl methyl carbonate (3:7) (Kishida Chemical Co., Ltd. Japan) were used, respectively. The cells were assembled in an Ar-filled glovebox. The cells were charged and discharged in advance within the potential range from 0.01 to 2.5 V at an approximate 0.1 C current rate before the operando measurement. Because the Li was used as a counter electrode, the graphite electrode was positive within this cell system. However, we describe Li intercalation into graphite as "charging" and Li deintercalation as "discharging" for consistency with practical full-cell-type rechargeable Li-ion batteries. Then, SXD, ^{7}Li-NMR and Raman measurements were performed at a current rate of 0.1 CA (for 10 h) in the range from 0.01 to 2.5 V. The cell structures and measurement methods are described as follows.

Operando SXD measurement.—An Al-laminated half-cell with dimensions of 70 × 70 mm^2 composed of graphite and Li electrodes (20 × 20 mm^2) was assembled with the electrolyte mentioned above (Fig. 2A). SXD measurements were performed during the second charge/discharge cycle at BL28XU in the Super Photon ring-8 (SPring-8), Japan. The SXD diffraction profiles were acquired every 10 s and approximately 7200 profiles were obtained during the charge/discharge process. The detailed operando measurement conditions have already been reported.[28]

Operando ^{7}Li-NMR measurement.—Figure 2B shows a two-electrode laminate cell that was specially designed for the ^{7}Li-NMR measurement. A polyethylene film was used as the laminate material to enclose a three-layer assembly consisting of the graphite and Li electrodes (5 × 15 mm^2) and a separator with the electrolyte. Electrochemical operando ^{7}Li-NMR measurements were performed with a homemade wide-bore static probe with a 10-mm-diameter solenoid coil using a DD2 600 spectrometer (Agilent Technologies, Inc.) in which the laminate cell was placed at the centre of the solenoid coil and oriented perpendicular to the magnetic field. The cell was cycled under the same charge/discharge conditions used for SXD. The spectra were acquired every 1 min at a resonance frequency of 233 MHz for ^{7}Li during the charge/discharge process and approximately 1200 spectra were obtained. The ^{7}Li chemical shifts were referenced to the 1 M LiCl solution at 0.0 ppm.

Operando Raman spectra measurement.—For Raman spectroscopy, a commercially available cell (SB6, EC Frontier Co., Ltd.) was used (Fig. 2C). The same electrode materials and electrolyte used in the SXD and ^{7}Li-NMR measurements were used for the cell configuration. The charge/discharge conditions were also the same as those used in the SXD and ^{7}Li-NMR measurements. Raman spectra were measured using an NRS-3100 spectrometer (JASCO Corp.) with an excitation wavelength of 532 nm. The spectra were acquired every 1 min and approximately 1200 spectra were obtained. Because of the decomposition of the charge/discharge products due to long-term laser irradiation, the observation area during discharge was changed from that observed during charging; additionally, only spectra measured in the range below 20% of the SOC were used to reduce the influence of decomposition. In the measurements, the vibration frequency of the in-plane Raman-active mode, called the G-band (E_{2g2} (ca.1580 cm^{-1})), was mainly measured. The G-band profile is strongly affected by the intercalation. The graphite exhibits a singlet G-band. However, it exhibits a doublet band with stage

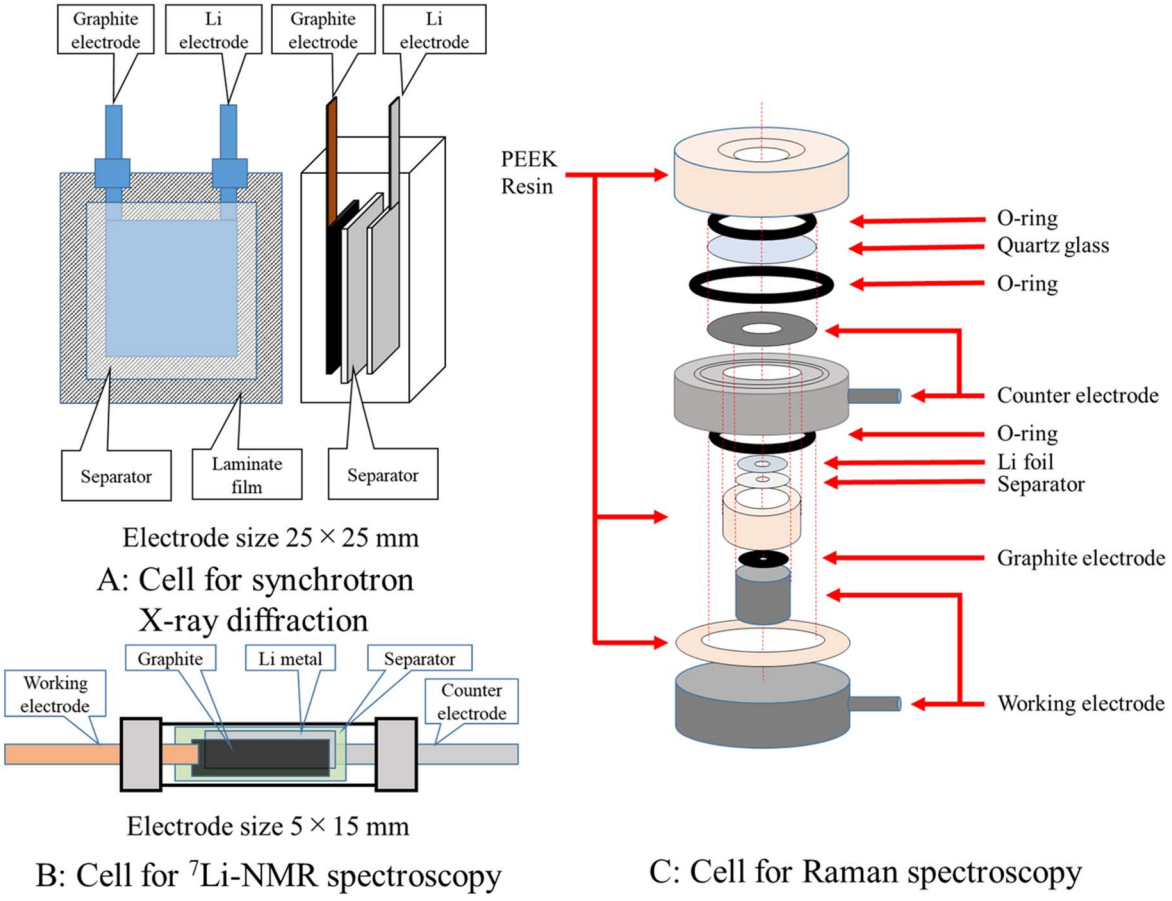

Figure 2. Schematic diagrams of the three types of laminate cell used for the SXD, ^{7}Li-NMR and Raman spectroscopy measurements. Although the cell structures differ from each other, the same positive and negative electrodes, separators, and electrolyte were used in each case.

n Li-GIC > 2, because two graphene sheet types that are in contact with and not in contact with the intercalant are formed, as shown in Fig. A·1. However, in the case where $n \leqslant 2$, all graphene sheets are contact with the intercalant and the G-band exhibits a singlet again. Therefore, when the Li ions intercalate/deintercalate into/from graphite, a profile change from singlet to doublet or doublet to singlet, respectively, must occur at some point during the process; this is very important for analysis of the reaction mechanism. To assess this phenomenon, G-band variations for graphite were monitored as a function of the composition x of LiC_x.

Concept of synchronized operando analysis.—Above-mentioned experiments yielded approximately 7200 SXD profiles and 1200 spectra for the ^{7}Li-NMR and Raman measurements. Each operando dataset was measured independently under the same charge/discharge conditions. Profile changes can thus be analysed synchronously as a function of the LiC_x composition calculated from the cumulative coulombic amount Q. To analyse this dataset, "Profile Chaser" analysis software was developed in Windows 10 (Fig. 3). This software enables tracking of profile changes in the 002, 100 and 101 diffractions, NMR signals and G-band Raman signal of graphite simultaneously and synchronously with the charge/discharge curves, the differential curves (V-dQ/dV) and the LiC_x compositions. First, the 002 diffraction profile changes make it possible to capture the various structural change stages. Second, the in-plane structure formation process can be captured from the 100 diffraction changes. Third, the AB stacking ↔ AA stacking sequence transition point can be determined from the 101 diffraction changes (Fig. A·2). The ^{7}Li-NMR chemical shift indicates formation of LiC_{6n} and LiC_{9n} compounds. The G-band Raman shift enables stage change recognition. Using the software, all profile changes during the charge/discharge processes were uploaded to a computer. The profiles were displayed on a monitor as a series in conjunction with compositions estimated from the charge/discharge curves, allowing profile changes to be tracked visually.

Results and Discussion

Synchronized analysis of SXD and ^{7}Li-NMR.—Figure 4A shows the ^{7}Li-NMR spectrum changes for every 1% of the state of charge (SOC) during charging. Figures 4B and 4C show SXD profile changes measured under the same conditions. Figures 5A–5D show the ^{7}Li-NMR chemical shifts and d_{100} and d_{002} value changes as a function of x in LiC_x. In the ^{7}Li-NMR results, peaks A and B were observed at $x > 22$ at $\delta = 5$–15 ppm and at $x < 22$ at $\delta = 40$–45 ppm, respectively; the former shifted towards higher magnetic fields as the Li concentration decreased. Letellier et al.[14] and Chevallier et al.[15] assigned these signals to LiC_{9n} and LiC_{6n}, respectively. Peak C, which is observed around $\delta = 80$–90 ppm, is a satellite of peak B. In Fig. 5A, this peak shows a clear inflection point in the chemical shift near $x = 9$, i.e. at $\delta = 80$ ppm when $x > 9$ and $\delta = 90$ ppm when $x < 9$. Because this represents an intermediate composition between stages 2 (LiC_{12}) and 1 (LiC_6), we conclude that this satellite peak reflects the transition from stage 2 to stage 1. As illustrated in Fig. 5C, formation of stage 1 was observed from approximately $x = 9$ in the d value composition dependence estimated from SXD, demonstrating extremely good agreement between the measurements. When the transition from stage 2 to stage 1 occurs, expansion occurs not only in the c-axis direction but also in the a, b-axes directions. In particular, a new 110 diffraction of stage 1 appears at $d = 0.2157$ nm as shown in Fig. 4B. Geometrically and crystallographically, d_{110} is related to the C=C bond length, $d_{C=C}$ by $d_{C=C} = 2/3d_{110}$ that constitutes the six-membered

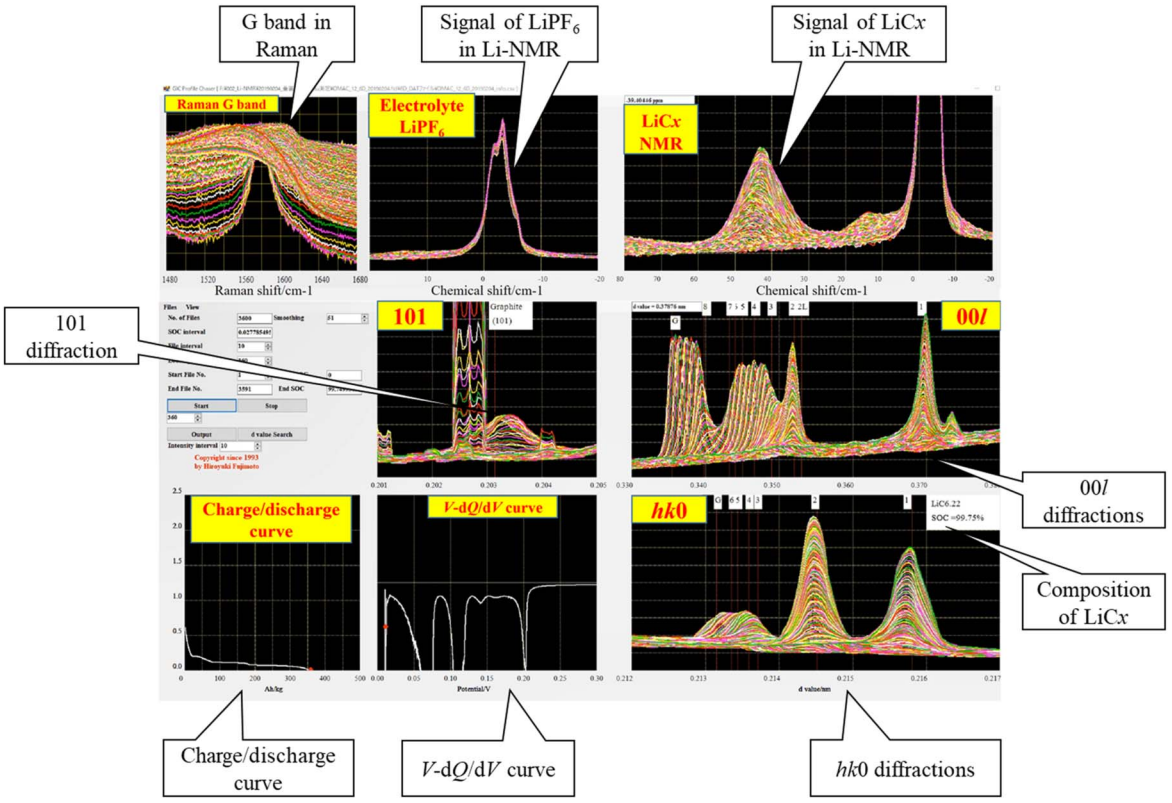

Figure 3. Profile chaser user interface. Three types of operando dataset from SXD, ^{7}Li-NMR and Raman spectra were analysed synchronously with the charge/discharge curves, their V-dQ/dV curves and the composition LiC_x.

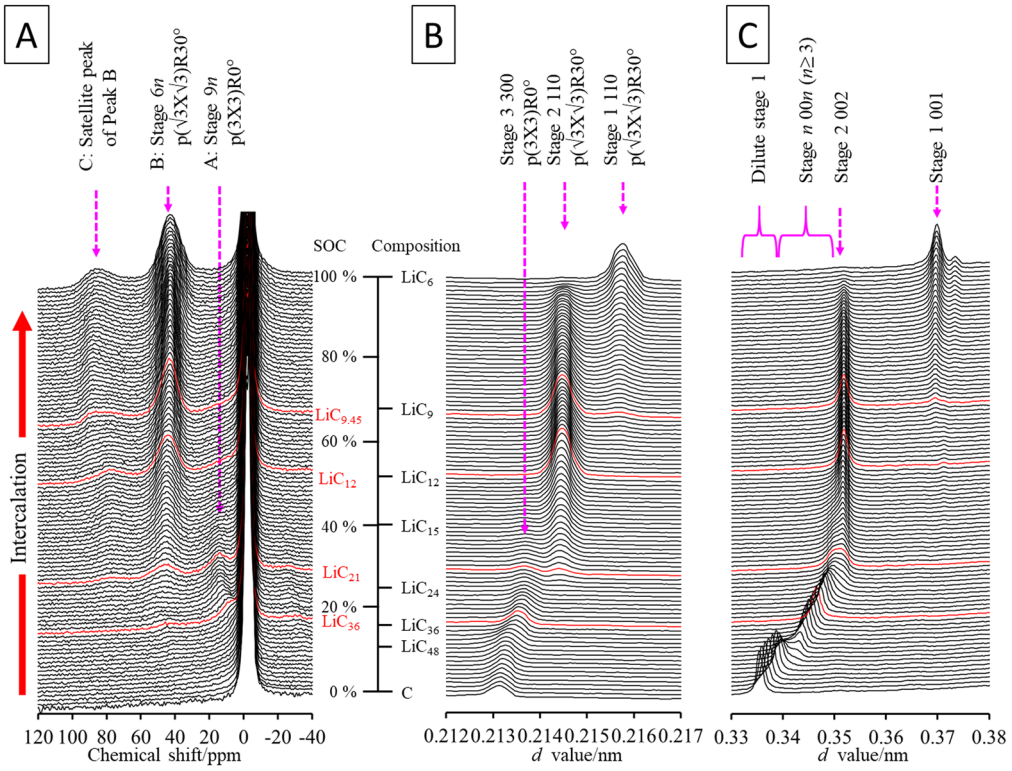

Figure 4. Dynamic changes in (A) ^{7}Li-NMR spectra and (B) 100 and (C) 002 diffraction profiles of graphite during the charge process.

carbon rings in graphene. That is, when the 110 diffraction shifts to the higher value, the six-membered carbon ring expands by the increment of C=C bond length and the symmetry around the Li ion changes somewhat changes. The shift of the satellite peak is considered to capture this phenomenon. In contrast, the two diffraction lines observed at d = 0.2138 nm and 0.2145 nm in Fig. 4B are the 300 and 110

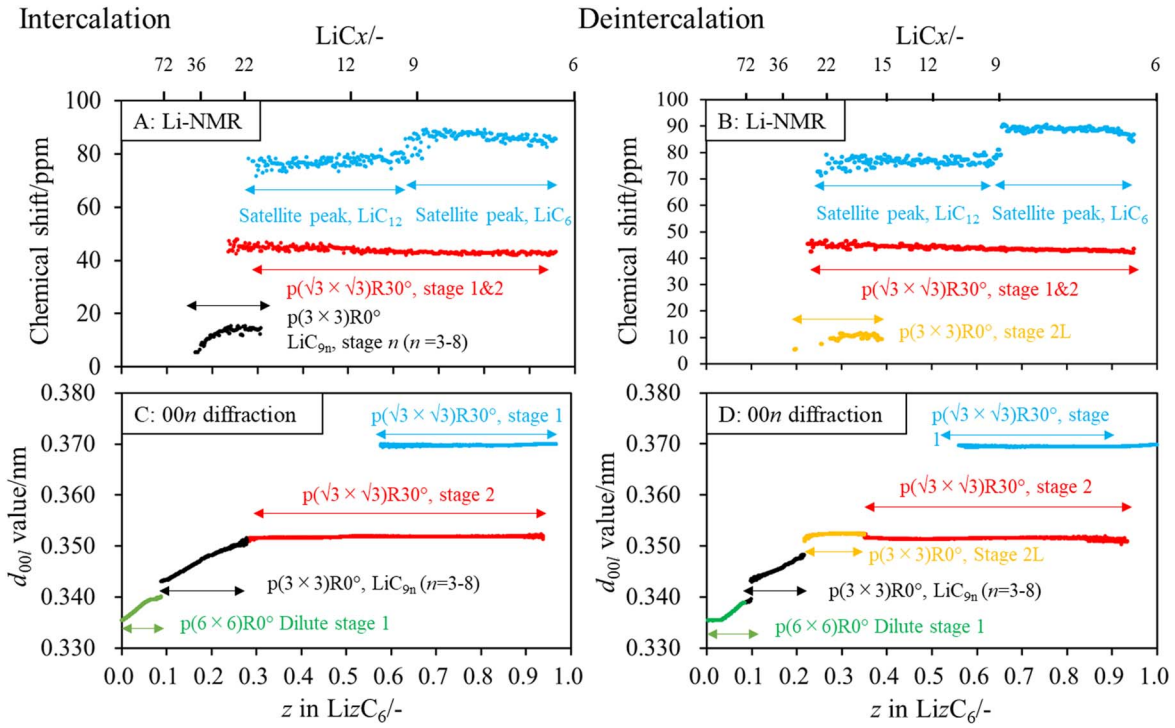

Figure 5. Chemical shifts in (A, B) ^{7}Li-NMR and (C, D) d values estimated from the ^{7}Li-NMR and SXD dataset as a function of x in LiC_x.

diffraction lines derived from the superlattice structures of LiC_9 (p(3 × 3)R0°) in stage 3 and LiC_6 (p(√3 × √3)R30°) in stage 2, respectively, and the transition between these structures appears near $x = 21$, as shown in the ^{7}Li-NMR spectra. The agreement between the ^{7}Li-NMR and SXD measurements indicated that peaks A and B in the ^{7}Li-NMR are derived from LiC_9 (p(3 × 3)R0°) and LiC_6 (p(√3 × √3)R30°)-type superlattice structures, respectively. Therefore, the results show that stage 1 and stage 2, which have identical in-plane structures, appear at almost the same position of $\delta = 40$–45 ppm, and higher stages above stage 3 then appear at $\delta = 5$–15 ppm. Billaud et al.[7] reported two stage 2 structure types with compositions of LiC_{12} and LiC_{18}; their average composition was thus LiC_{15}. In contrast, the stage 3 composition was LiC_{27}. Therefore, the structural transition between stages 2 and 3 will occur near $x = 21$. Peak A, which was assigned to LiC_{9n}, gradually shifted towards higher magnetic fields as x increased before finally overlapping with the $LiPF_6$ peak from the electrolyte, when it could not be recognized clearly.

Hysteresis in deintercalation process.—Comparison of Figs. 5A and 5B shows that the chemical shift changes in peaks B and C in the ^{7}Li-NMR spectra during deintercalation are almost identical to those during intercalation, while the phase transition between stages 1 and 2 proceeds almost reversibly. However, peak A's chemical shift during deintercalation differed from that observed during intercalation. The former signal showed $\delta < 12$ ppm within the $15 < x < 30$ composition range, while the latter showed $\delta < 15$ ppm in the $21 < x < 36$ range. This is a hysteresis characteristic; Yazami and Reynier[13] also reported this hysteresis. Similarly, in Fig. 5D, a new stage 2 with larger d value appears in the LiC_{15}–LiC_{30} composition range during deintercalation; this was designated liquid-type stage 2 l by Dahn.[9] Because the range in which diffraction occurs corresponds well with peak A of the ^{7}Li-NMR results, peak A is considered to correspond to stage 2l. However, stage 2l was not observed during intercalation, as illustrated in Fig. 5C.

Synchronized analysis of SXD and Raman.—Graphite consists of thousands of graphene sheets stacked in an AB structure (Fig. A·2), while the Li-GIC shows AA stacking.[2,3] Therefore, when Li ions intercalate/deintercalate into/from graphite, transitions from AB to AA or from AA to AB stacking, respectively, must occur during the reaction. To clarify this point, the change in the graphite 101 diffraction profile with d value of approximately 0.2031 nm was traced; the diffraction characteristic showed the three-dimensional regularity peculiar to AB stacking, i.e. the diffraction disappears after the intercalation-induced AB to AA transition. Figures 6A and 6B show the 101 and 002 diffraction profile changes during early intercalation, respectively. The broad peak at approximately 0.2031 nm is the 101 diffraction and several peaks at 0.202–0.203 nm are caused by Al-laminate film orientation changes during charging. As intercalation proceeded, the 101 diffraction intensity gradually decreased and almost disappeared within the $LiC_{72.0}$–$LiC_{63.0}$ composition range. This indicates that the graphite AB stacking was transformed into AA stacking when the $LiC_{63.0}$ composition was reached and that Li species had intercalated into all interlayers. Dilute stage 1 was thus formed. Simultaneously, the 002 diffraction intensity decreased while the d value increased gradually from 0.3354 nm to 0.34 nm, and the 002 peak finally split into a clear doublet in the $LiC_{72.0}$–$LiC_{63.0}$ range. Billaud et al.[7] proposed existence of a p(3 × 3)R0°-type superlattice with in-plane composition of LiC_9[7]. From their proposal, the stage 7 and 8 compositions should be LiC_{63} and LiC_{72}, respectively, and the 002 profile change during early intercalation is attributed to dilute stage 1 formation followed by a transition from dilute stage 1 via stage 8 (LiC_{72}) to stage 7 (LiC_{63}). The 002 profile of $LiC_{67.5}$ (Fig. A·3), which is the exact intermediate composition between stages 7 and 8, consists of two peaks with an almost 1:1 intensity ratio, while the $LiC_{67.5}$ 100 profile shows a single peak at approximately 0.2133 nm (Fig. A·3). This indicates that stages 7 and 8 have the same LiC_9-type in-plane structure. Figure 6C shows dynamic change in the graphite G-band (1580 cm^{-1}, vibration mode E_{2g2}) in the Raman spectra within the same composition range. During intercalation, the G-band shifted gradually from approximately 1578 cm^{-1} towards the higher frequency side (1590 cm^{-1}) up to a composition of LiC_{72}. SXD results indicate that this vibration change is due to slipping of AB-stacking into AA-stacking because of Li ion insertion. During the early reaction stage, Li ions are inserted between all layers to generate

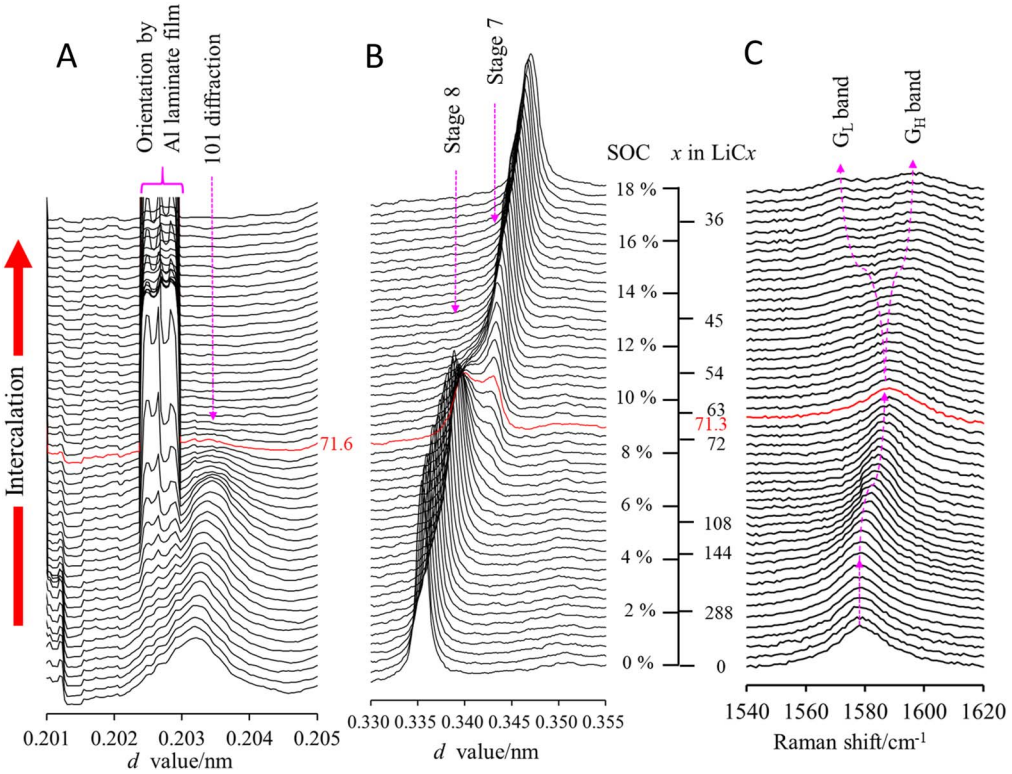

Figure 6. Dynamic changes in 101 and 002 diffractions and Raman spectra of graphite electrode in earlier intercalation process.

dilute stage 1, which causes a G-band to G_H-band transition. As a result, the G-band on which the generated G_H-band is superimposed causes broadening while gradually shifting towards the high frequency side. As the amount of dilute stage 1 formed increases, the initial G-band disappears and becomes a single peak in the G_H-band, thus changing into a sharp band again. As intercalation proceeds, Li rearrangement occurs between the interlayers, leading to stage 8 formation with an in-plane LiC_9 ($p(3 \times 3)R0°$) structure, and two graphene sheet types that are in contact or not in contact with the intercalant are formed (Fig. A·1). A dramatic change thus occurs in the vibration modes on both graphene sheet types and E_{2g2} splits into two bands, corresponding to the E^0_{2g2} (G_L-band) and $\hat{E}_{2g2}$ (G_H-band) vibration modes.[5,29–32] The former appears on a lower frequency side than the latter. Then, from the Daumas-Hérold model,[33–35] stage 8 transitions into lower stage compounds in order from stage 7 → stage 6 → stage 5 → stage 4. Solin reported that, for an alkali metal-GIC, the G_L-band shifts towards a lower frequency side than the G-band; this point is also consistent with their results.[5,29–32] The dynamic change in the Raman spectra also agreed well with the corresponding SXD profile changes in Figs. 6A and 6B.

Conclusions

We applied SXD, ^{7}Li-NMR and Raman spectroscopy to operando analysis of the graphite electrode charge/discharge mechanism in a Li-ion battery. Graphite electrode spectra were measured successively during the reaction. The operando dataset obtained was analysed synchronously with the x composition in LiC_x estimated from the charge/discharge curves. The most important aspect of this study is demonstration of a technique to track successive changes in SXD, ^{7}Li-NMR and Raman spectra simultaneously with the LiC_x composition. This provides information about C–C bond vibration mode behaviour and interactions between Li and carbon atoms due to structural changes during charge/discharge reactions. Synchronized analysis using SXD and Raman spectroscopy confirmed that the 002 diffraction and the G-band of graphite changed from singlet to doublet forms near LiC_{72}. This indicates that the dilute stage 1 saturation composition is LiC_{72} and it was concluded that Li rearrangement between the interlayers leads to stage 7 via stage 8. Synchronous analysis of SXD and ^{7}Li-NMR spectroscopy results showed that the transition from LiC_{9n} to LiC_{6n} occurs in the vicinity of $LiC_{21–22}$. Because the ^{7}Li-NMR and Raman measurements results show very good agreement with the SXD measurements, the intercalation mechanism shown in Fig. 1 can be explained conclusively.

Acknowledgments

This work was supported by the Research and Development Innovative for Scientific Innovation of New Generation Battery 2 (RISING2) project and the New Energy and Industrial Technology Development Organization (NEDO JPNP16001). The synchrotron radiation experiments were performed at the BL28XU in SPring-8 with the approval of the Japan Synchrotron Radiation Research Institute (JASRI) (Proposal Nos. 2016A7602, 2016B7603, 2017A7603, 2017B7603, 2018A7603, 2019A7613 and 2019B7613). We thank David MacDonald, MSc, from Edanz (https://www.edanz.com/ac) for editing a draft of this manuscript.

Appendix A

A.1. The stage structure change of Li-GIC.—The stage structure changes of Li-GIC occur in the order from dilute stage 1 → stage 8 → stage 7 → stage 6 → stage 5 → stage 4 → stage 3 → stage 2 → stage 1 as shown in Fig. A·1.

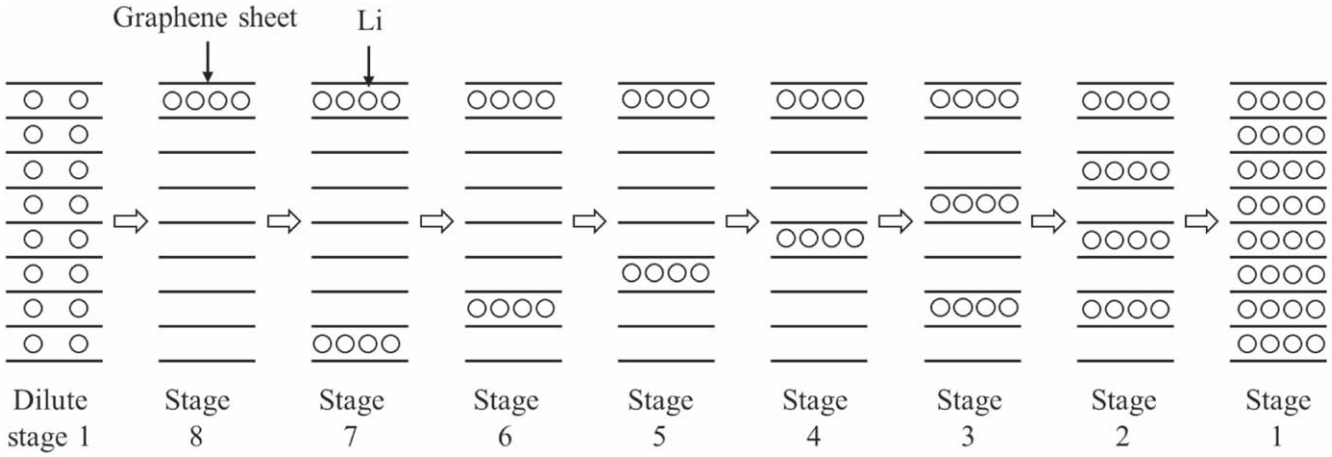

Figure A·1. Schematic diagrams of the stage structure change of Li-GIC.

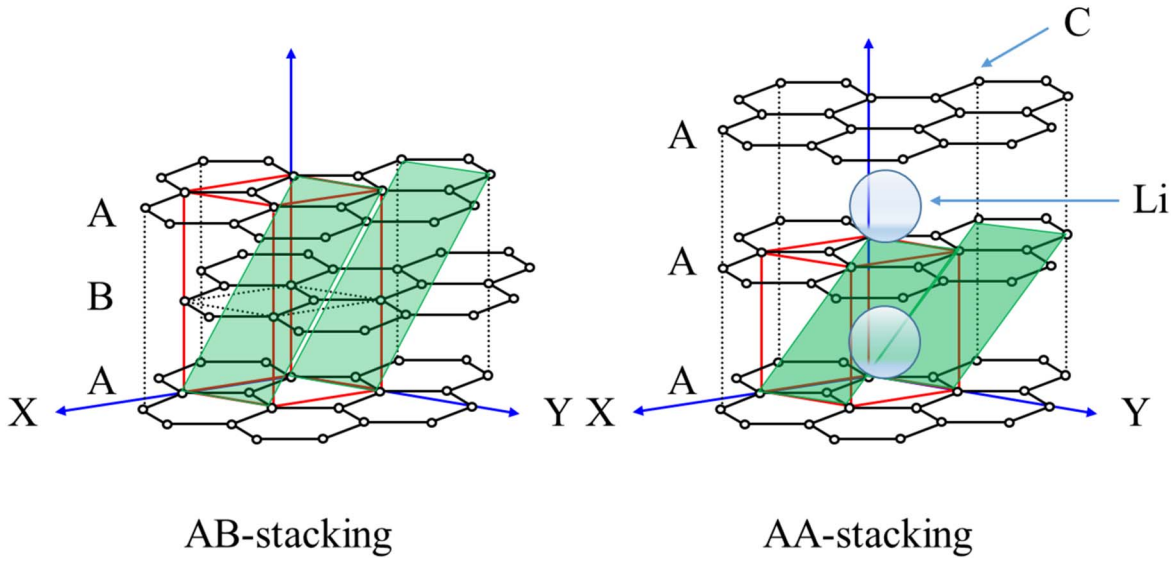

Figure A·2. Stacking sequences of graphite (AB-stacking) and Li-GIC (AA-stacking).

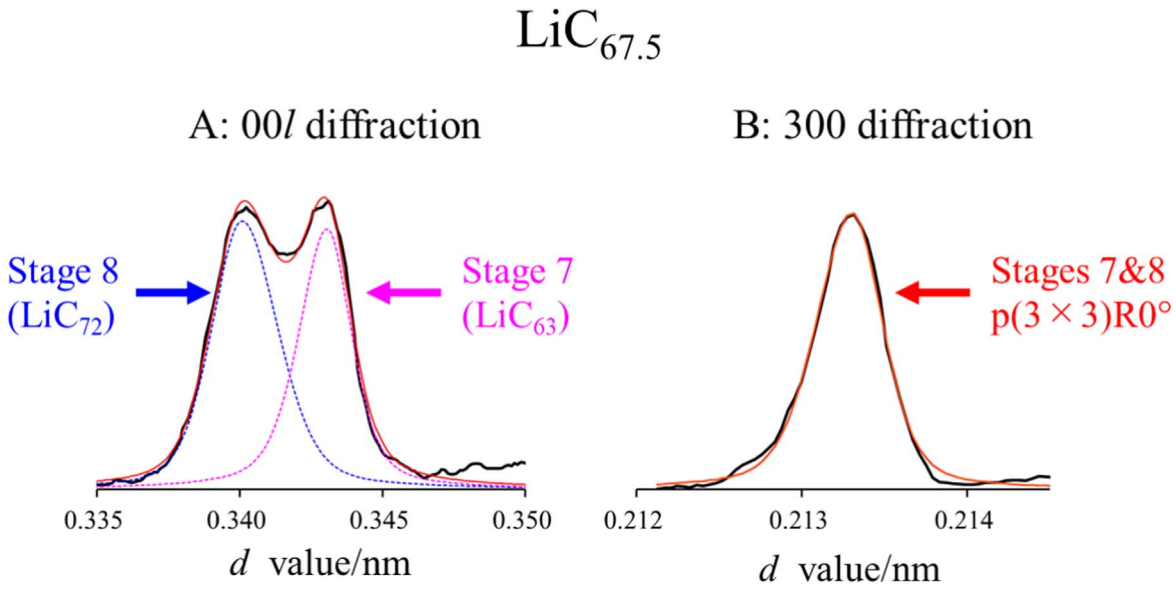

Figure A·3. 00*l* and 300 diffraction profiles of $LiC_{67.5}$. The 00*l* profile of $LiC_{67.5}$ in A, which is the exact intermediate composition between stages 7 and 8, consists of two peaks with an almost 1:1 intensity ratio, while the 100 profile of $LiC_{67.5}$ shows only a single peak at approximately 0.2133 nm (B). This indicates that stages 7 and 8 have the same LiC_9-type in-plane structure.

Appendix B

B.1. Stacking sequences of graphite (AB-stacking) and Li-GIC (AA-stacking).—The red line framework shows the unit cell in each case. The pairs of green planes show the 101 reflections. Graphite consists of thousands of graphene sheets stacked in an AB structure, while the Li-GIC has an AA stacking structure. When a Li ion intercalates/ deintercalates into/from graphite, the transition from AB to AA or from AA to AB stacking, respectively, must occur at some point during the reaction. To clarify this point, the change in the 101 diffraction profile of graphite, which has a d value of approximately 0.2031 nm, was traced; this diffraction profile shows the three-dimensional regularity peculiar to AB stacking, i.e. the diffraction disappears after the transition from AB to AA induced by intercalation.

ORCID

Hiroyuki Fujimoto https://orcid.org/0000-0003-4562-7715

References

1. A. Hérold and B. Soc, *Chim. France*, **187**, 999 (1955).
2. D. Guerard and A. Hérold, *Carbon*, **13**, 337 (1975).
3. N. Kambe, M. S. Dresselhaus, G. Dresselhaus, S. Basu, A. R. McGhie, and J. E. Fischer, *Mat. Sci. Eng.*, **40**, 1 (1979).
4. D. Gerard, M. Chaabouni, P. Lagrange, M. E. Makrini, and A. Hérold, *Carbon*, **18**, 257 (1980).
5. M. S. Dresselhaus and G. Dresselhaus, *Adv. Phys.*, **30**, 139 (1981).
6. N. Emery, C. Hérold, and P. Lagrange, *Prog. Solid State Chem.*, **36**, 213 (2008).
7. D. Billaud, E. McRae, J. F. Mareche, and A. Hérold, *Synth. Met.*, **3**, 21 (1981).
8. S. B. Dicenzo, S. Basu, and G. K. Werthem, *Synth. Met.*, **3**, 139 (1981).
9. J. R. Dahn, *Phys. Rev. B*, **44**, 9170 (1991).
10. M. Inaba, H. Yoshida, Z. Ogumi, T. Abe, Y. Mizutani, and M. Asano, *J. Electrochem. Soc.*, **142**, 20 (1995).
11. T. Ohzuku, Y. Iwakoshi, and K. Sawai, *J. Electrochem. Soc.*, **140**, 2490 (1993).
12. K. Zaghib, K. Tatsumi, Y. Sawada, S. Higuchi, H. Abe, and T. Ohsaki, *J. Electrochem. Soc.*, **146**, 2784 (1999).
13. R. Yazami and Y. Reynier, *J. Power Sources,*, **153**, 312 (2006).
14. M. Letellier, F. Chevallier, and M. Morcrette, *Carbon*, **45**, 1025 (2007).
15. F. Chevallier, F. Poli, B. Montigny, and M. Letellier, *Carbon*, **61**, 140 (2013).
16. A. Senyshyn, M. J. Mühlbauer, K. Nikolowski, T. Pirling, and H. Ehrenberg, *J. Power Sources,*, **203**, 126 (2012).
17. A. Senyshyn, O. Dolotko, M. J. Mühlbauer, K. Nikolowski, H. Fuess, and H. Ehrenberg, *J. Electrochem. Soc.*, **160**, A3198 (2013).
18. H. He, C. Huang, C. W. Luo, J. J. Liu, and Z. S. Chao, *Electrochim. Acta*, **92**, 148 (2013).
19. N. Sharma and V. K. Peterson, *Electrochim. Acta*, **101**, 79 (2013).
20. L. Cai, K. An, Z. Feng, C. Liang, and S. J. Harris, *J. Power Sources,*, **236**, 163 (2013).
21. N. Sharma and V. K. Peterson, *J. Power Sources,*, **244**, 695 (2013).
22. O. Dolotko, A. Senyshyn, M. J. Mühlbauer, K. Nikolowski, and H. Ehrenberg, *J. Power Sources,*, **255**, 197 (2014).
23. V. Zinth, C. Lüders, M. Hofmann, J. Hattendorff, I. Buchberger, S. Erhard, J. R. Kornmeier, A. Jossen, and R. Gilles, *J. Power Sources,*, **271**, 152 (2014).
24. H. Park, M. Kim, F. Xu, C. Jung, S. M. Hong, and C. M. Koo, *J. Power Sources,*, **283**, 68 (2015).
25. J. K. Mathiesen, R. E. Johnsen, A. S. Blennow, and P. Norby, *Carbon*, **153**, 347 (2019).
26. S. A. Krachkovskiy, J. M. Foster, J. D. Bazak, B. J. Balcom, and G. R. Goward, *J. Phys. Chem. C*, **122**, 21784 (2018).
27. A. I. Freytag, A. D. Pauric, S. A. Krachkovskiy, and G. R. Goward, *J. Am. Chem. Soc.*, **141**, 13758 (2019).
28. H. Fujimoto, H. Kiuchi, S. Takagi, K. Shimoda, K. Okazaki, Z. Ogumi, and T. Abe, *J. Electrochem. Soc.*, **168**, 040509 (2021).
29. M. S. Dresselhaus, G. Dresselhaus, P. C. Eklund, and D. D. L. Chung, *Mat. Sci. Eng.*, **31**, 141 (1977).
30. S. A. Solin, *Mat. Sci. Eng.*, **31**, 153 (1977).
31. R. J. Nemanich, G. Lucovsky, and S. A. Solin, *Mat. Sci. Eng.*, **31**, 157 (1977).
32. S. A. Solin, *Physica*, **99B**, 443 (1980).
33. N. Daumas and A. Hérold, *C. R. Acad. Sci. Ser. C*, **268**, 373 (1969).
34. S. Krishnan, G. Brenet, E. M. Charry, D. Caliste, L. Genovese, T. Deutsch, and P. Pochet, *Appl. Phys. Lett.*, **103**, 251904 (2013).
35. E. M. G. Arriazu, O. A. Pinto, B. A. L. Mishima, D. E. Barraco, O. A. Oviedo, and E. P. M. Leiva, *Electrochem. Commun.*, **93**, 133 (2018).